High-temperature ramsdellite–pyrolusite transformation kinetics

(Article begins on next page)

ORIGINAL PAPER

High-temperature ramsdellite–pyrolusite transformation kinetics

Nadia Curetti[1] · **Davide Bernasconi[1]** · **Piera Benna[1]** · **Gianluca Fiore[2]** · **Alessandro Pavese[1]**

Abstract

The two most common polymorphs of MnO_2, ramsdellite and pyrolusite, are often found in natural association. Our starting sample is from the Mistake mine (Arizona) containing macroscopic crystals of both ramsdellite ($a = 4.5131(6)$, $b = 9.2689(13)$, $c = 2.8610(4)$ Å, $V = 119.69(3)$ Å^3; S.G. *Pbmn*) and pyrolusite ($a = 4.4030(2)$, $c = 2.87392(16)$ Å, $V = 55.715(5)$ Å^3; S.G. *P4$_2$/mnm*), along with a smaller amount of "groutellite". A mixed powder was used to study the ramsdellite→pyrolusite transformation by in situ high-temperature X-ray powder diffraction. Our results reveal that this transformation is not a direct transition, but it occurs in two steps, as a function of temperature; ramsdellite transforms into an amorphous phase, which then recrystallizes into pyrolusite. Amorphization of ramsdellite and crystallization of pyrolusite kinetics were studied by the universal equation for solid–solid reactions. The two activation energies are comparable, but the pre-exponential factor of the ramsdellite amorphization is two orders of magnitude larger than pyrolusite crystallization's. As a consequence, ramsdellite→pyrolusite transformation implies the formation of an amorphous transition, due to a mismatch between the conversion rates, that reaches its maximum at around 630 K and then decreases at higher T, when pyrolusite crystallization is strongly promoted.

Keywords MnO_2 polymorphs · High-temperature transformation · Reaction kinetics · Pyrolusite · Ramsdellite

Introduction

Manganese is the 12th most abundant element in the Earth's crust and second only to iron among the most common heavy metals (Emsley 2001). Extensive depositions of Mn–oxide occur in the oceans as nodules, micro-concretions, coatings and crusts (Crerar and Barnes 1974). Mn–oxides are of interest because they give rise to different structural arrangements and magnetic phases. The building block shared by these structures is the octahedron, MnO_6. In nature, MnO_2 stabilizes three polymorphs (pyrolusite, ramsdellite and nsutite), whose structures are based on octahedral chains along [001].

*Pyrolusite (β-MnO_2; rutile-type structure, S.G. *P4$_2$/mnm*)* is the most common and stable polymorph of MnO_2. Its structure (Kondrashev and Zaslavskii 1951; Wyckoff 1963;

Bolzan et al. 1997) is comprised of octahedral chains, interlinked by shared corners, so that they form a framework exhibiting square cross-sectional tunnels along [001] (Fig. 1a).

*Ramsdellite (R-MnO_2; S.G. *Pbnm*)* is a rare mineral, isostructural with diaspore (AlOOH) and goethite (FeOOH) (Ramsdell 1932; Fleischer and Richmond 1943; Miura et al. 1990; Fong and Kennedy 1994), whose structure is characterized by edge-sharing double octahedral chains along [001], which are interconnected to each other via sharing of corners. Such an arrangement leads to the formation of tunnels with rectangular cross-sections (Fig. 1c).

Nsutite (from the large deposits near Nsuta, Ghana) is a disordered intergrowth between pyrolusite and ramsdellite (Turner and Buseck 1983). The synthetic analogue, referred to by the acronym EMD (electrolytic Mn dioxide), is widely employed in battery production as a cathodic material. Its tunnel structure allows solid-state diffusion of protons, and Mn can take several valence states, thereby affecting the force field that influences diffusion (Balachandran et al. 2002).

In all MnO_2 polymorphs it is observed that, if a fraction of Mn^{4+} reduces to Mn^{3+}, then H^+ and/or Li^+ are allowed

✉ Nadia Curetti
  nadia.curetti@unito.it

1 Earth Sciences Department, University of Torino, Via Valperga Caluso 35, 10125 Torino, Italy

2 Department of Chemistry, University of Torino, Via Pietro Giuria 7, 10125 Torino, Italy

Fig. 1 Structural framework of pyrolusite and ramsdellite. The unit-cells are shown. Pyrolusite (S.G. $P4_2/mnm$): **a** the octahedral chains disposed along z; **b** the shape of the MnO_6 octahedron is quite regular. The two *axial* $Mn–O_{ax}$ bonds, perpendicular to the (110) plane, have length R_1 and the four *equatorial* $Mn–O_{eq}$ bonds have length R_2. Ramsdellite (S.G. *Pbnm*): **c** couples of octahedral chains disposed along z, edge-sharing ($O_2–O_2$) connected by corners (O1); **d** the MnO_6 octahedron is distorted.
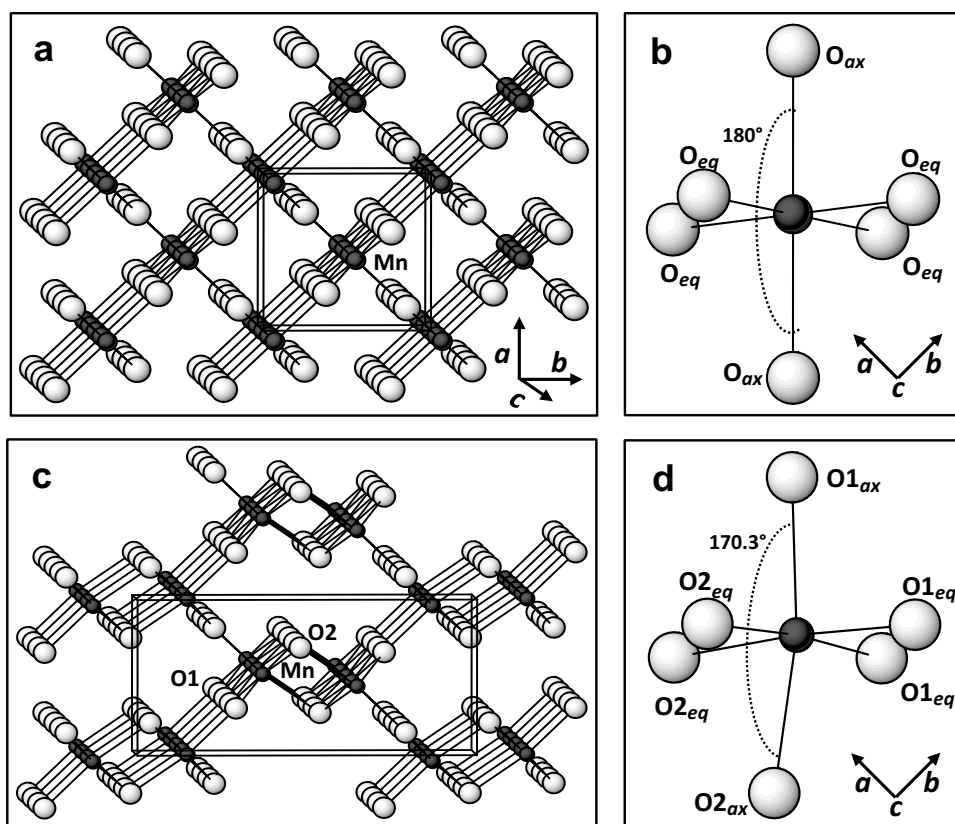
to enter the tunnel framework to guarantee charge balance (Zachau-Christiansen et al. 1994; Chabre and Pannetier 1995; MacLean et al. 1995; MacLean and Tye 1996). The protonation of pyrolusite and ramsdellite generates manganite and groutite respectively, both with chemical formula MnOOH (Post and Heaney 2004). Mn^{3+} and H^+, in turn, induce Jahn–Teller distortions affecting the Mn–coordinated octahedron (Kohler et al. 1997). In addition, along the ramsdellite–groutite joint lies "groutellite", which shares the structure with ramsdellite (and groutite), unless that the hydroxyl group replaces half oxygen atoms abutting the tunnels (Klingsberg and Roy 1959), thus leading to a chemical formula given by $(Mn^{4+}_{0.5} Mn^{3+}_{0.5}) O_{1.5} (OH)_{0.5}$. Although "groutellite" has not been approved as a mineral by the CNMNC Commission (International Mineralogical Association), we shall use this term without quotations hereafter, for the sake of brevity.

Ramsdellite is highly sensitive to heating (Bernardini et al. 2020), and all the more so groutellite. The latter completely transforms into ramsdellite in air at $T \sim 513–573$ K (Post and Heaney 2004), owing to oxidation of manganese passing from Mn^{3+} to Mn^{4+}, which implies a H^+ loss. The thermal behavior of ramsdellite was studied by Fleischer et al. (1962), who observed a full conversion into pyrolusite through a 5-days treatment at 583 K. Post and Heaney (2004) performed in situ high-temperature experiments, which

showed an anomalous behavior of the unit-cell volume (it increases up to 425 K, then decreases to 530 K and at higher T increases again) and suggested placing the onset of the phase transition to pyrolusite at 590 K. Kennedy (2019) investigated the changes of the structure of pyrolusite up to 673 K by high-resolution synchrotron X-ray powder diffraction. The results reveal that the unit-cell expansion is weakly anisotropic ($\alpha_c = 7.2 \times 10^{-6}$ K^{-1} and $\alpha_a = 7.8 \times 10^{-6}$ K^{-1}): the two axial M–O bond distances slightly increase with T, whereas the four equatorial M–O bonds seem independent of T. At about 903 K, a process of de-oxygenation takes place in pyrolusite, leading to the formation of a non-crystalline oxide ($Mn^{2+}_2 Mn^{4+}_3 O_8$), which transforms into a bixbyite-like (α-Mn_2O_3) material at about 973 K, and at higher temperatures into a hausmannite-like oxide ($Mn^{2+}Mn^{3+}_2O_4$; Zaki et al. 1997).

Although there is general agreement about the temperature of the ramsdellite→pyrolusite transition, much is still unknown about the reaction kinetics driving such a transformation. There are two reasons, in our opinion, to pay attention to this topic:

(i) from earlier investigations, we gather that the mechanism governing the ramsdellite→pyrolusite conversion involves a re-arrangement of the crystal structure into an amorphous phase, from which re-

crystallization then takes place. This case of a two-stage reaction is of interest for the different kinetic processes that are involved, and affect the transformation;

(ii) pyrolusite and ramsdellite provide a two-phase material with a bearing on the battery production, and the key-properties depend on the proportions of the mentioned phases. Therefore, a full control of the reaction leading from one to the other plays a part in designing a suitable mixture in view of intended applications.

In this light, we undertook the present work, whose aim is of elucidating the reaction kinetics of the ramsdellite→pyrolusite transformation and look into its evolution stages, paying special attention to distinguish between collapse kinetics of ramsdellite and successive crystallization kinetics into pyrolusite.

Experimental

Characterization of the sample

The sample under investigation (from M. Ciriotti Collection; Russo 2007) comes from Mistake Mine, Sam Powell Peak, Yavapai County, Arizona (Wilkinson et al. 1983). It is a black mass of about $4 \times 3 \times 3$ cm, covered by macroscopic MnO_2-crystals (> 300 μm). X-ray powder diffraction revealed the occurrence of pyrolusite, ramsdellite and groutellite (the latter probably fine grained, because no single crystal was found).

Pyrolusite and ramsdellite exhibit either simultaneous growth or partial transformation from one into the other. Both polymorphs appear opaque or silver-black, thus making difficult any optical determination; yet, they can be distinguished from one another because of morphology. In fact, we observed pyrolusite crystals of acicular morphology (see also Fleischer et al. 1962), in contrast with the ramsdellite's stocky habit. Several single crystals were selected and tested by preliminary X-ray diffraction, to identify the polymorph. Some of the examined crystals were embedded in araldite, polished and carbon coated, for chemical composition determination that was carried out by means of a JEOL JSM-IT300LV Scanning Electron Microprobe, equipped with Oxford INCA Energy 200 EDS SATW detector (WD 10, KV 15). The composition of either polymorph was determined as the average of 15 independent analyses, on three different specimens.

Single-crystal X-ray diffraction (SC-XRD)

We selected one single crystal of pyrolusite (PYR) and four of ramsdellite (RAM1/2/3/4), for full X-ray diffraction data collections. Measurements were performed by a Gemini R Ultra (Rigaku-Oxford Technologies, MoKα radiation, X-ray generator at 50 kV and 40 mA, detector distance 53 mm), equipped with Atlas CCD detector (CrisDi Center, University of Torino). Diffraction intensities were recorded up to a 2θ-angle of 90°, with a width angle of 1°. In the case of ramsdellite, data reduction yielded reflections of intensity larger than 3σ up to 70° 2θ, only.

The 171-39-46 version of CrysAlisPro software (Rigaku—Oxford Technologies) was used to measure and integrate the reflection intensities, and to account for absorption and Lorentz-polarization corrections. Structure refinements were carried out by SHELX-97 Package (Sheldrick 2008), using the space groups $P4_2/mnm$ and $Pbnm$ for pyrolusite and ramsdellite, respectively. In the case of ramsdellite, three settings are possible: $Pbnm$ (Byström 1949), $Pnma$ (Post and Heaney 2004) and $Pnam$ (Kondrashev and Zaslavskii 1951). We chose the first one, so as to have the octahedron chains along [001], as in pyrolusite.

Measurement conditions and results from structure refinements are reported in Table 1, for pyrolusite (PYR) and ramsdellite (RAM2); CSD codes 2091767–2091771 contain the supplementary crystallographic data for all the crystals here investigated (PYR, RAM1/2/3/4). These data can be obtained free of charge via https://www.ccdc.cam.ac.uk/.

Powder X-ray diffraction (XRPD)

Powders were treated with 1 M acetic acid solution, to dissolve carbonate (calcite) and remove it from the sample. Preliminary XRPD measurements were performed using a Rigaku MiniFlex 600 powder diffractometer with Bragg–Brentano geometry and CuKα radiation (tube operating at 40 kV and 15 mA), to recognise all the occurring phases. In doing so, we observed pyrolusite, ramsdellite and groutellite.

Thereafter, we performed in situ high temperature (HT) XRPD data collections, both at equilibrium/quasi-equilibrium (data collections at given T, after achievement of equilibrium) and non-equilibrium conditions (data collections at different times and given T, with reaction in progress). Such measurements were carried out using a Rigaku SmartLab XE diffractometer (Bregg-Brentano θ–θ geometry, CuKα radiation, generator operating at 40 kV and 30 mA) equipped with Rigaku Multipurpose High Temperature Attachment, combined with PTC-EVO temperature control. The sample was placed in a basin-like platinum sample-holder equipped with vertical Pt-flakes, to maintain a uniform T at the sample. The actual temperature at the sample was

Table 1 Unit-cell parameters, measurement conditions and refinement results of single crystals X-ray diffraction on pyrolusite (PYR) and ramsdellite (RAM2) at room conditions

	PYR		RAM2
a (Å)	4.4030(2)	a (Å)	4.5131(6)
b (Å)	–	b (Å)	9.2689(13)
c (Å)	2.87392(16)	c (Å)	2.8610(4)
V (Å^3)	55.715(5)	V (Å^3)	119.69(3)
Refl. cell	1582	Refl. cell	404
min θ (°)	6.51	min θ (°)	4.40
max θ (°)	44.59	max θ (°)	36.83
S.G.	$P4_2/mnm$	S.G.	$Pbnm$
Total refl.	3915	Total refl.	1768
Unique refl.	148	Unique refl.	341
R (%) $F_0 \geq 4\sigma(F_0)$	2.40	R (%) $F_0 \geq 4\sigma(F_0)$	4.45
R (%) all	2.88	R (%) all	6.08
wR^2 (%)	6.08	wR^2 (%)	9.07
Goodness of fit	1.16	Goodness of fit	1.16
Refin. Param.	8	Refin. Param.	19
Mn–O$_{ax}$ (Å) (×2)	1.9006(15)	Mn–O1$_{ax}$ (Å)	1.889(3)
		Mn–O2$_{ax}$ (Å)	1.912(3)
Mn–O$_{eq}$ (Å) (×4)	1.8803(10)	Mn–O1$_{eq}$ (Å) (×2)	1.880(2)
		Mn–O2$_{eq}$ (Å) (×2)	1.911(1)
<Mn–O>	1.8871(5)	<Mn–O>	1.8972(9)
O$_{eq}$-O$_{eq}$ (Å)	2.8739(2)	O1$_{eq}$-O1$_{eq}$ (Å)	2.8610(4)
	2.425(3)	O1$_{eq}$-O2$_{eq}$ (Å)	2.482(5)
O$_{ax}$–Mn–O$_{eq}$ (°)	90	O1$_{ax}$–Mn–O1$_{eq}$ (°)	92.67(4)
	–	O1$_{ax}$–Mn–O2$_{eq}$ (°)	91.96(11)
	–	O2$_{ax}$–Mn–O1$_{eq}$ (°)	93.52(12)
	–	O2$_{ax}$–Mn–O2$_{eq}$ (°)	81.80(11)
O$_{ax}$–Mn–O$_{ax}$ (°)	180	O1$_{ax}$–Mn–O2$_{ax}$ (°)	170.45(14)
O$_{eq}$–Mn–O$_{eq}$ (°)	99.67(7)	O1$_{eq}$–Mn–O1$_{eq}$ (°)	99.12(15)
	–	O2$_{eq}$–Mn–O2$_{eq}$ (°)	96.91(14)
O$_{eq}$–Mn–O$_{eq}$ (°)	80.33(7)	O1$_{eq}$–Mn–O2$_{eq}$ (°)	81.75(12)
CSD Depos. Num.	2091767	CSD Depos. Num.	2091770

determined through a calibration curve, previously obtained using solid–solid phase transitions (quartz and Na_2SO_4) and dilatation of standard materials (metallic Si and Pt), up to about 1300 K.

High-temperature XRPD measurement at equilibrium/quasi-equilibrium conditions

Quartz (20 wt%) was added as an internal standard to the sample. The room temperature XRPD pattern was used as reference. The sample was heated at a rate of 10 K/min up to a given T. Data collections at T started after awaiting 30 min to achieve equilibrium. We used a 256-channel multi-strip detector moving with a speed of 0.5°/min, in the range $10 < 2\theta < 110°$ at steps of 0.01° (about 200 min for

each data collection). XRPD patterns were recorded every 10 K up to 493 K (Fig. 2), then larger T-steps were used. We employed the GSAS-II Software Package (Toby and Von Dreele 2013) for full profile fitting, adopting pseudo-Voigt profile functions to model the experimental patterns. We chose a refinement strategy based on varying the phase proportions, the profile function parameters associated with grain size and strain, the coefficients of the Chebyshev polynomial linear combination that describes the background. We did not refine structure parameters, using those from the present work (pyrolusite and ramsdellite) or from literature (groutellite: Post and Heaney 2004; quartz as an internal standard: Gualtieri 2000; platinum of the sample holder: Hu et al. 2011). Instrumental contributions to the peak shape, such as asymmetry and intrinsic peak broadening, were determined by means of a standard sample (LaB_6). The relative intensity of the peaks did not suggest occurrence of preferred orientation of the crystallites in the sample.

The amounts of pyrolusite, ramsdellite, groutellite and amorphous phase at different temperature were determined using the added quartz (20 wt%) as an internal standard. Amorphous phase was quantified by re-scaling the proportions of the crystal phases to reproduce the known amount of quartz.

### XRPD measurement at constant temperature—kinetics

Measurements were carried out at 588, 603, 623, 633 and 658 K, using a CCD detector (Rigaku Hypix 3000) to speed up recording. The CCD detector was positioned at 25° in 2θ, to collect diffraction signals on the range $17 < 2\theta < 32°$. The exposure time was set to 20 s and data collections were carried out every fifth minute. We converted the raw diffraction images into 2θ-intensity patterns, whose peak areas were calculated by the software Fityk 0.9.8 (Wojdyr 2010) and used to model the thermal transformation of the occurring phases. The narrow 2θ range we explored allowed us to collect patterns suited to measure the changes of phase composition involving ramsdellite and pyrolusite, but insufficient for application of the Rietveld analysis. Therefore, we focused our attention on following the integrated intensity of the two main Bragg peaks of the polymorphs, as a function of time.

Results and discussion

Structures of pyrolusite and ramsdellite at room conditions

Pyrolusite and ramsdellite samples share the same observed chemical composition that, within the experimental

Fig. 2 Diffraction pattern at $T = 574$ K; vertical bars mark the diffraction position of the phases. High low-angle background is due to the camera used for in situ *HT* measurements (Multipurpose System—Rigaku Technology). The refinement converges to the following figures of merit: $wR = 5.04\%$ on 9501 observations, $R = 3.32\%$, R-bkg $= 5.89\%$, Goodness of fit $= 1.98$
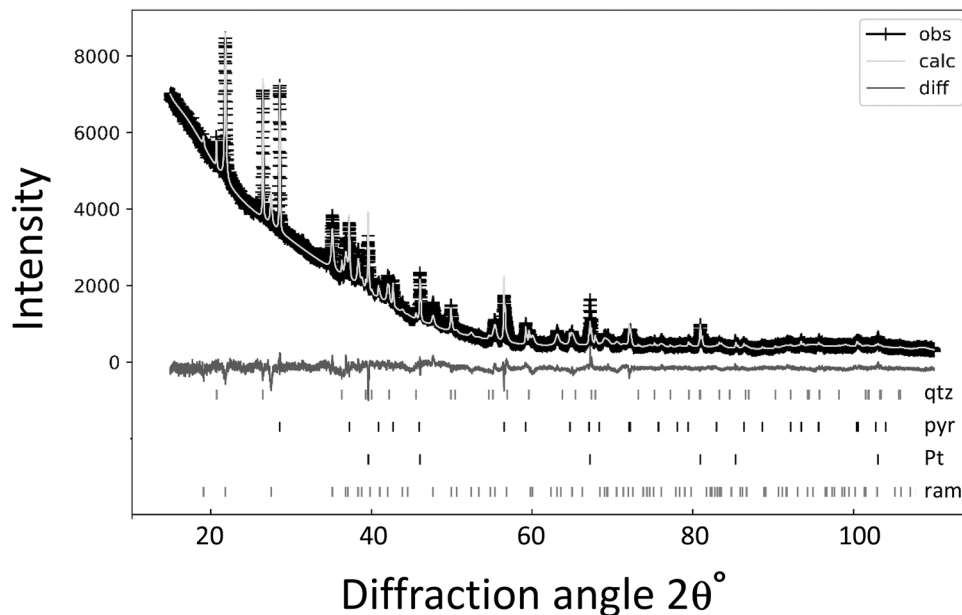
uncertainties, can be approximated to the pure substances, i.e. MnO_2.

The pyrolusite single crystal under study exhibits a high degree of order and its structure refinement converges to a figure of merit as good as $R = 2.40\%$ (Table 1). Unit-cell parameters and x atomic coordinate of oxygen (the only structural degree of freedom) agree with those reported in previous works (Kondrashev and Zaslavskii 1951; Wyckoff 1963; Curetti et al. 2019). The measured difference between *axial* and *equatorial* Mn–O bond lengths, $R_1 = 1.9006(15)$ and $R_2 = 1.8803(10)$ Å, is small, but the commonly observed inequality $R_1 > R_2$ is confirmed.

The degree of structural order in ramsdellite crystals (RAM1/2/3/4) is lower than pyrolusite's, and the refinements converge to figures of merit in the range 4.45–6.10%. The unit-cell parameters (Table 1) are comparable to those reported by Byström (1949) and by Post and Heaney (2004). As we mentioned in "Introduction", when the structural channels host H^+, Li^+ or Ca^{2+}, the b parameter increases remarkably because of the induced Jahn–Teller distortion, even related to the ionic radius size of Mn^{3+} larger than Mn^{4+}, as shown by Post and Heaney (2004). In our case, ramsdellite exhibits a b that agrees with the values reported in literature, and there is no evidence of any Mn^{4+} reduction.

In ramsdellite, the shape of the octahedron is more distorted than in pyrolusite, because the orthorhombic symmetry allows more degrees of freedom, and there are two independent sites hosting O1 and O2, which provide the octahedral coordination of Mn (Fig. 1c, d). The average < Mn–O1 > bond distance is shorter than < Mn–O2 > (Table 1), and the following inequalities hold: Mn–O1$_{ax}$ > Mn–O1$_{eq}$ and Mn–O2$_{ax}$ > Mn–O2$_{eq}$. The average < Mn–O > bond distance is slightly longer in ramsdellite than in pyrolusite, because O2 is more distant from Mn than O1: the O2's site lies adjacent to the open-tunnels into which the occupying oxygen can easily relax.

## Transformation of ramsdellite to pyrolusite— kinetic evolution

Quasi-equilibrium

We explored the thermal range from 300 to 765 K, waiting ~ 30 min before data recording. We were not able to perform reliable Rietveld structure refinements, because of the number of phases involved; however, we refined the unit-cell parameters of all phases at each T, along with profile broadening parameters and phase proportions. The latter allowed us to follow the transformation

Table 2 Results of the $\ln(-\ln(1-\alpha))$ vs $\ln t$ analysis

Phase	T (K)	n	R^2
Ramsdellite	588	0.6	0.97
	603	0.63	0.95
	623	0.91	0.99
	633	0.88	0.97
	658	0.86	0.97
		0.78 (average)	
Pyrolusite	623	0.89	0.98
	633	0.76	0.97
	658	0.96	0.99
		0.87 (average)	

Fig. 3 Relative amounts of pyrolusite, ramsdellite, groutellite and amorphous phase at different temperature, calculated on the base of internal quartz; the weight percentages of the crystalline phases were rescaled on the base of the known quartz (20 wt%) and the amount of amorphous was derived as the difference from 100%. ESD's bars are ± 3sigma
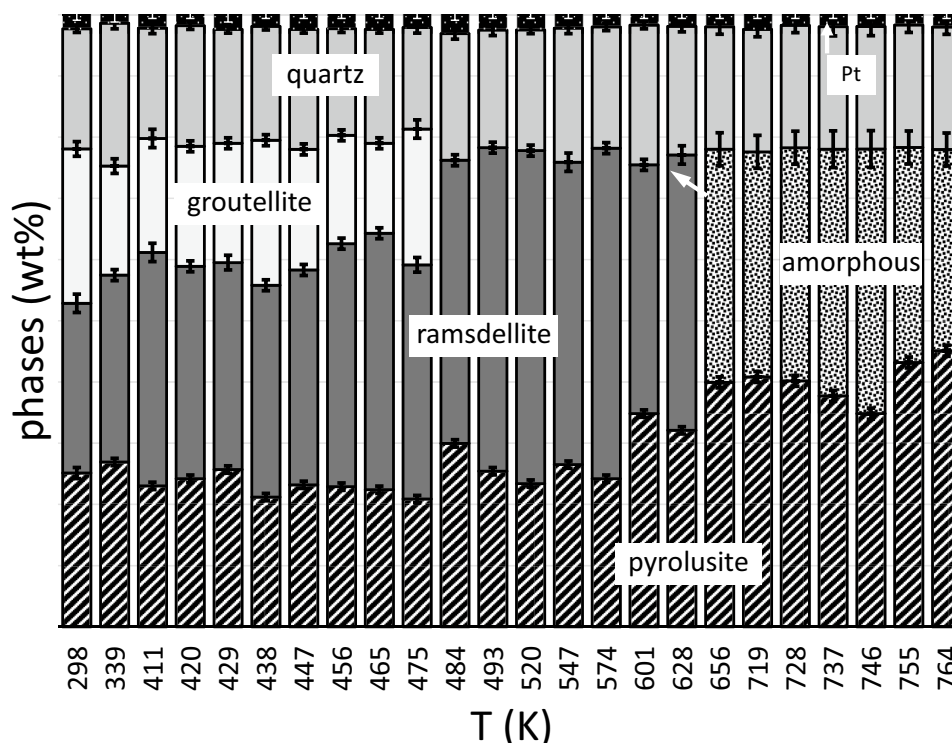
of the minerals in the mixture under investigation (Table 2; Fig. 3). We exploited the contribution of platinum from the sample-holder to the diffraction patterns as an additional inner reference. Pt, treated as an independent "virtual" phase, was estimated as abundant as ~ 2 wt%, at room temperature. At H*T*, Rietveld profile refinements, in which the phase proportions are varied, yielded figures of Pt-abundance ranging from 1.4 to 2.4, with an average of 2.1(4) wt%, in full agreement with determinations at room conditions (note that the effect of deprotonation in groutellite is negligible). α-Quartz, which is stable on the investigated *T* range, was estimated as much as 20 wt%; refinements yielded figures between 17 and 23 wt%, with an average of 19.7(1). This made us confident about the reliability of the phase composition that can be obtained from profile analysis, and thus we chose to use quartz as an internal standard. Up to 475 K, we observe the same phases that occur at room temperature; at 486 K, groutellite disappears transforming into ramsdellite, as suggested by an increase of the latter. Such a transformation results from a combination of Mn–oxidation ($Mn^{3+} \rightarrow Mn^{4+}$) and O–H bond collapse (the latter associated with a mobilization of H^+), as is documented in a previous work using high-temperature IR spectroscopy (Post and Heaney 2004). This reaction does not require recrystallization, as both three-dimensional structure framework and related bonds are preserved. The phase proportions change negligibly up to ~ 600 K; beyond, one appreciates an increase of pyrolusite and at ~ 656 K ramsdellite's diffraction peaks

disappear, and an amorphous phase develops, into which ramsdellite has at least partially been converted. The specimen at ~ 628 K may contain some amorphous phase, but pattern analysis does not highlight this.

Therefore, we approximate the formal onset of the transition from ramsdellite to pyrolusite at about 600 K, in agreement with Post and Heaney (2004) who claim a start above 590 K.

The transition from ramsdellite to pyrolusite has been observed and described by earlier authors as an irreversible transformation (Fleischer et al. 1962; Post and Heaney 2004). Our data show that this change takes place passing through an amorphous state followed by subsequent recrystallization, in keeping with the fact that no relation of group/sub-group holds between ramsdellite and pyrolusite space groups.

Kinetics

In this light, the ramsdellite→pyrolusite transformation is governed by the relations between the reaction kinetics of ramsdellite amorphization and pyrolusite crystallization. The intensity of the 1 1 0 peak (2θ = 21.9°) was used to follow the progressive amorphization of ramsdellite along chosen isotherms. For each set of measurements at constant *T*, we calculated the conversion fraction (α) as a function of time, using the formula reported below:

$$\alpha = \frac{(I_0 - I_t)}{(I_0 - I_\infty)}, \tag{1a}$$

where I_0, I_t and I_∞ are the integrated intensities of the 1 1 0 peak at the beginning of the process (*i.e.*, its maximum intensity), at time t and at an "infinite" time (such that the reaction can be considered as "completed"), respectively. Note that, α increases with decrease of ramsdellite, which is somewhat counterintuitive. Yet, such a relationship correctly describes the nature of the reaction that actually consists of a progressive disappearance of a crystal phase. The isothermal plots of α versus t infer that ramsdellite's amorphization reaction follows a "decelerator" model (Khawam and Flanagan 2006), i.e. the reaction rate decreases with the reaction progress (Fig. 4a).

In the case of pyrolusite formation, we used the 1 1 0 peak integrated intensity ($2\theta = 28.7°$) to track down the crystallization reaction. In particular, given that pyrolusite is present in the mixture before the reaction takes place, we employed a conversion fraction defined as follows:

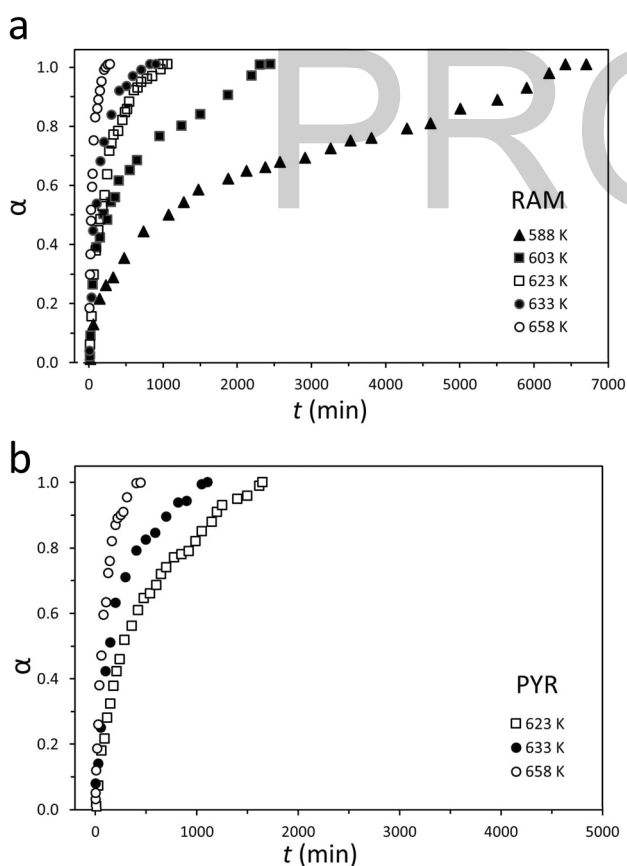$$\alpha = \frac{(I_t - I_0)}{(I_0 - I_\infty)}. \tag{1b}$$

a

b

Fig. 4 The conversion fraction α as a function of time for **a** five isothermal runs in ramsdellite (RAM, 588, 603, 623, 633, 658 K) and **b** three isothermal runs in pyrolusite (PYR, 623, 633, 658 K)

In contrast with Eq. (1a), the equation above provides an α parameter that does increase with the increase of pyrolusite amount.

Both conversion fractions, given by Eq. (1a) and (1b), are such that $\alpha \rightarrow 1$ upon approaching the completion of the related reaction, whether of amorphization or of crystallization. Also, pyrolusite crystallization agrees with a "decelerator" model, as shown by its $\alpha - t$ plot (Fig. 4b).

The kinetic parameters that drive isothermal solid–solid transformations can be related to a universal equation accounting for both nucleation and growth, *i.e.* the formulation of Avrami (1939) and Johnson and Mehl (1939), which results in

$$ln(-ln(1 - \alpha)) = n \times ln(k) + n \times ln(t), \tag{2}$$

where k is the rate constant of the reaction (it depends on the frequency of nucleation and the growth rate of the grains), and n is the order of the reaction. This model was originally developed to study growth kinetics of new phases that are supposedly not present at the beginning of the process. However, the satisfactory agreement we observed in fitting the model above to our experimental data made us confident in using Eq. (2).

Figure 5 shows the interpolations of α versus t, according to the equation above. Using the slope and intercept of the linear fitting, we were able to calculate n and k for each set of isothermal curves. In particular, the resulting values of n help constrain the kinetic model that is most appropriate to fit our data. As shown in Table 2, ramsdellite amorphization yields n of 0.78, while pyrolusite formation gives 0.87. Such figures hint that these reactions are likely the diffusion-controlled type (Hancock and Sharp 1972). The $ln(k)$ term, in turn, was fitted as a function of $1/T$ (Arrhenius plot) and exhibits a linear trend (Fig. 6). We used the fundamental relationships

$$k = Ae^{-\frac{E_a}{RT}}, \tag{3a}$$

$$\ln(k) = \ln(A) - \frac{E_a}{RT}, \tag{3b}$$

where A and E_a are the pre-exponential, or frequency, factor and (apparent) activation energy, respectively, associated with the observed $k(T)$ values.

There is debate in literature about the physical meaning attributable to the parameters A and E_a of Eq. (3.a), when they are employed in solid–solid reactions (Galwey and Brown 2002; Galwey 2006; L'vov 2017). Batiot et al. (2021) provide a thorough analysis of the nature of the Arrhenius-type form of the rate constant, using a general approach relying on fundamentals of statistical mechanics. Altogether, the idea is commonly shared that a transformation from B to C is related to the occurrence of an
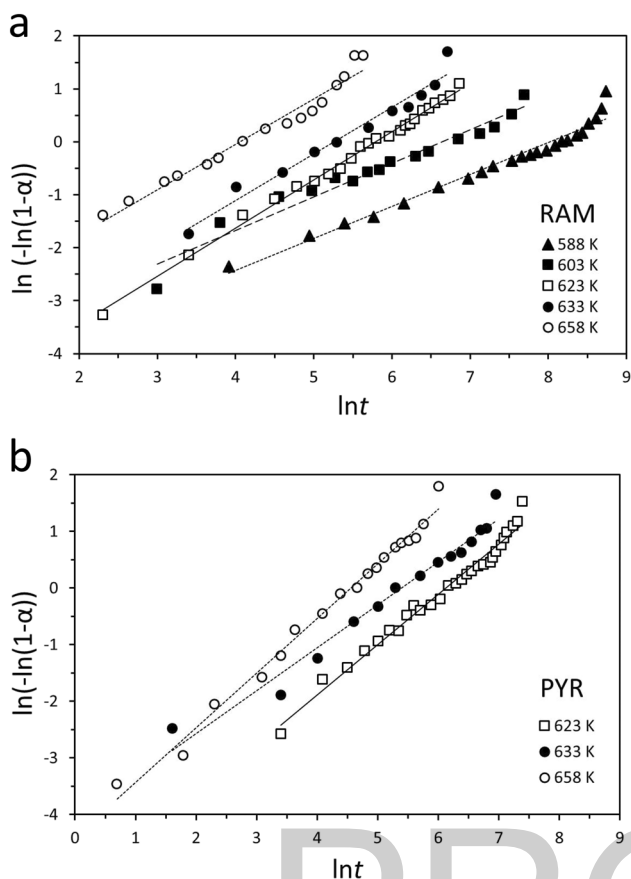
Fig. 5 Plot of $\ln(-\ln(1-\alpha))$ versus $\ln t$ for **a** five isothermal runs in ramsdellite (RAM, 588, 603, 623, 633, 658 K) and **b** three isothermal runs in pyrolusite (PYR, 623, 633, 658 K)
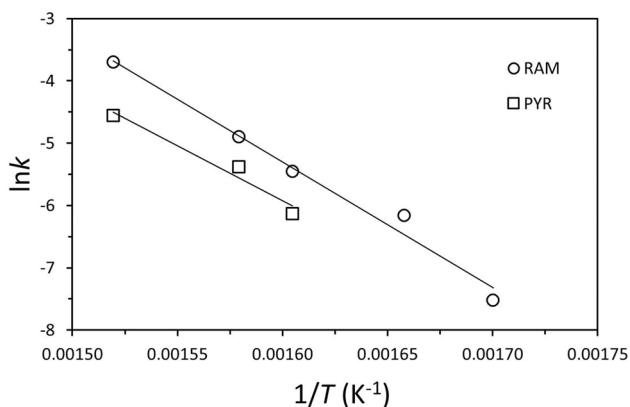

Fig. 6 Arrhenius plot for ramsdellite (RAM) and pyrolusite (PYR)

activated state (complex) $B^{\ddagger}$ that is intermediate between the other two. In this view, E_a is associated with the enthalpy (approximated by "energy" at room pressure) difference between $B^{\ddagger}$ and B, that is somewhat equivalent to an "energy barrier" to be overcome. The pre-exponential

factor, A, is of less straightforward interpretation, being related to the partition functions of B, $B^{\ddagger}$ and the reaction rate $B \rightarrow B^{\ddagger}$. Nevertheless, A can ultimately be linked to the notion of "frequency of occurrence" of the key mechanism triggering a transformation; for instance, in the case of gases it is a frequency of collision; for solids, we envisage a frequency of bond breaking, that is related to the atomic vibration (phonon) sufficient to extract atoms from their sites and mobilize them, thus leading to a structure readjustment.

The results are set out in Table 3. We found activation energy values of 167.7 and 146.5 kJ/mol, for ramsdellite (collapse) and pyrolusite (crystallization), respectively. Both values have never been reported in the literature to-date, to our knowledge. Zaki et al. (1997) studied the decomposition of pyrolusite and found that it takes place in the range 823–873 K, with an activation energy of 208.72 kJ/mol.

Using the parameters of Tables 2 and 3, and the relationship below

$$\alpha = 1 - e^{-k(T)t^n}, \tag{4}$$

we calculated the ratio $\alpha(t)_{RAM}/\alpha(t)_{PYR}$, at a given temperature and as a function of time (Fig. 7), where $\alpha(t)_{RAM}$ and $\alpha(t)_{PYR}$ are the conversion fractions for ramsdellite amorphization and pyrolusite crystallization, respectively.

In doing so, we emphasize the effect induced by the different kinetics of either reaction (i.e. collapse and crystallization) on the whole transformation process.

In particular, $\alpha(t)_{RAM}/\alpha(t)_{PYR}$ exhibits a decreasing trend, peaking at the initial stage of the reaction and then asymptotically approaching unity, which indicates completion of the ramsdellite $\rightarrow$ pyrolusite transformation. This trend is particularly sensitive to the pre-exponential factor, A, which is two order of magnitude greater for ramsdellite amorphization than pyrolusite crystallization; the other kinetic parameters (i.e. E_a and n) of the two reactions are comparable to each other and become dominant in driving the reaction at high temperature. As a consequence, an

Table 3 Results of the Arrhenius analysis

Phase	T (K)	$\ln k$	E_a (kJ/mol)	A (min^{-1})	R^2
Ramsdellite	588	− 7.52	167.7	5.2×10^{11}	0.98
	603	− 6.16			
	623	− 5.45			
	633	− 4.9			
	658	− 3.7			
Pyrolusite	623	− 6.14	146.5	4.72×10^{9}	0.96
	633	− 5.38			
	658	− 4.56			

Fig. 7 The rate constants $\alpha_{RAM}/\alpha_{PYR}$ in ramsdellite and pyrolusite as a function of time in three isothermal runs ($T = 623$, 633, 658 K)
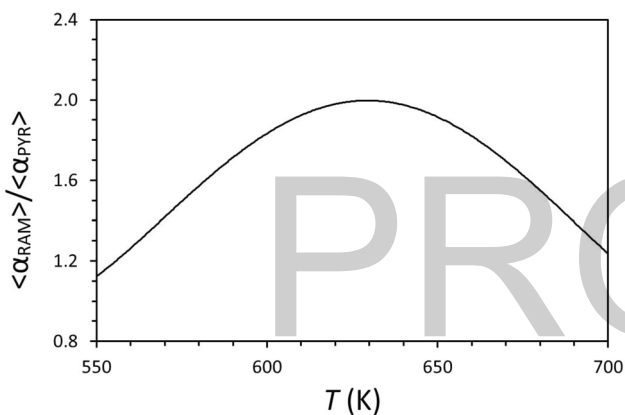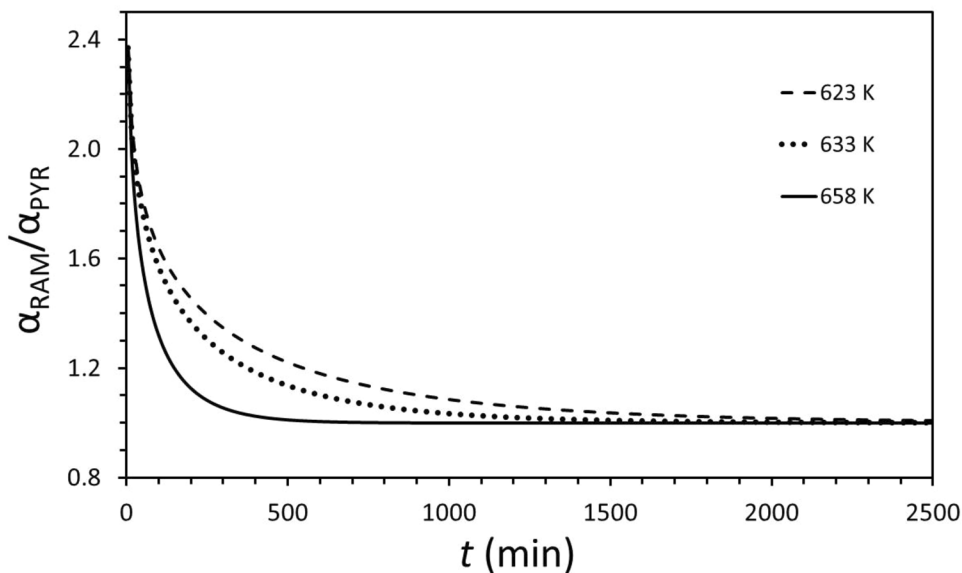

Fig. 8 The mean $\alpha_{RAM}/\alpha_{PYR}$ ratio at given T in ramsdellite and pyrolusite as a function of temperature, over a fixed time (i.e. 200 min)

"accumulation" of amorphous matter from the ramsdellite's collapse occurs, owing to the difference between the reaction rates of amorphization and crystallization.

All this is further stressed by Fig. 8 that displays the average $\alpha_{RAM}/\alpha_{PYR}$ over a 200 min time interval (*i.e.* full XRPD data collection time at equilibrium/quasi-equilibrium conditions), at a given temperature. It is clear from Fig. 8 that the above-mentioned discrepancy between the two reaction rates is dependent on T, and reaches its maximum at ~ 630 K, where the amount of amorphous phase starts becoming reliably quantifiable (Fig. 3). All this means that at such a temperature the largest kinetic difference between ramsdellite amorphization and pyrolusite crystallization is revealed, thus allowing an unambiguous detection of the amorphous fraction. Even at $T < 630$ K it is likely the occurrence of an amorphous component,

which we estimated by the kinetic model discussed above in terms of a few percent by weight, leaving aside any claim of precision.

Conclusions

The irreversible transformation of ramsdellite to pyrolusite at high temperature is known and reported in previous works. In the present work, our purpose is to elucidate the kinetic features of the two involved reactions: amorphization of ramsdellite and subsequent crystallization of pyrolusite. The results allow us to conclude:

– the transformation is not a direct phase transition, but it does occur through the appearance of an intermediate amorphous phase. In fact, ramsdellite collapses into an amorphous phase (onset about 600 K), from which pyrolusite crystallizes. The full transformation is observed to stretch from 600 to 660 K. In this light, the total transformation results in a balance of two distinct reactions;

– either reaction (ramsdellite amorphization and pyrolusite crystallization) can be described with the "decelerator" model of the universal equation of solid–solid transformations at constant T. The activation energy values of the two reactions are comparable to one another (E_a(amorphization) = 167.7 kJ/mol; E_a(crystallization) = 146.5 kJ/mol); conversely, the pre-exponential factors differ by two orders of magnitude (A(amorphization) = 5.2×10^{11} min^{-1}; A(crystallization) = 4.72×10^9 min^{-1}). As a consequence, the reaction rate of pyrolusite crystallization is smaller than amorphization (at ~ 630 K, this difference achieves its maximum), thus

inducing an "accumulation" of amorphous phase resulting from ramsdellite crystal structure collapse;

– as to the pristine natural sample used in the present investigation, the co-existence of pyrolusite and ramsdellite is supposed not to be an incomplete transformation (in such a case, we expect to find also amorphous component, which conversely is lacking), but the effect of an independent formation of either phase, perhaps owing to local variations of the crystallization conditions.

Availability of data and material The supplementary crystallographic data have been deposited.

Code availability CSD codes 2091767–2091771 contain the supplementary crystallographic data. These data can be obtained free of charge via https://www.ccdc.cam.ac.uk/ or from the Cambridge Crystallographic Data Centre, 12 Union Road, Cambridge CB2 1EZ, UK; e-mail: deposit@ccdc.cam.ac.uk.

Declarations

Conflict of interest The authors declare no conflicts of interest.

References

Avrami M (1939) Kinetics of phase change. I. General theory. J Chem Phys 7:1103–1112. https://doi.org/10.1063/1.1750380

Balachandran D, Morgan D, Ceder G (2002) First principles study of H-insertion in MnO$_2$. J Solid State Chem 166:91–103. https://doi.org/10.1006/jssc.2002.9564

Batiot B, Rogaume T, Richard F, Luche J, Collin A, Guillaume E, Torero JL (2021) Origin and justification of the use of the Arrhenius relation to represent the reaction rate of the thermal decomposition of a solid. Appl Sci 11(9):4075. https://doi.org/10.3390/app11094075

Bernardini S, Bellatreccia F, Della Ventura G, Ballirano P, Sodo A (2020) Raman spectroscopy and laser-induced degradation of groutellite and ramsdellite, two cathode materials of technological interest. RSC Adv 10:923–929. https://doi.org/10.1039/c9ra08662e

Bolzan AA, Fong C, Kennedy BJ, Howard CJ (1997) Structural studies of rutile-type metal dioxides. Acta Cryst B53:373–380. https://doi.org/10.1107/S0108768197001468

Byström AM (1949) The crystal structure of ramsdellite, an orthorhombic modification of MnO$_2$. Acta Chem Scand 3:163–173. https://doi.org/10.3891/acta.chem.scand.03-0163

Chabre Y, Pannetier J (1995) Structural and electrochemical properties of the proton/γ-MnO$_2$ system. Progr Solid State Chem 23:1–130. https://doi.org/10.1016/0079-6786(94)00005-2

Crerar DA, Barnes HL (1974) Deposition of deep-sea manganese nodules. Geochim Cosmoch Acta 38:279–300. https://doi.org/10.1016/0016-7037(74)90111-2

Curetti N, Merli M, Capella S, Benna P, Pavese A (2019) Low pressure ferroelastic phase transition in rutile-type AX$_2$ minerals: cassiterite (SnO$_2$), pyrolusite (MnO$_2$) and sellaite (MgF$_2$). Phys Chem Miner 46:987–1002. https://doi.org/10.1007/s00269-019-01057-7

Emsley J (2001) Manganese. Nature's building blocks: an A-Z guide to the elements. Oxford University Press, Oxford, pp 249–253 (**ISBN 978-0-19-850340-8**)

Fleischer M, Richmond WE (1943) The manganese oxide minerals: a preliminary report. Econ Geol SEG 38:269–286. https://doi.org/10.2113/gsecongeo.38.4.269

Fleischer M, Richmond WE, Evans HT (1962) Studies of the manganese oxides. V. Ramsdellite, MnO$_2$, an orthorhombic dimorph of pyrolusite. Am Miner 47:47–58

Fong C, Kennedy BJ (1994) A powder neutron diffraction study of λ and γ manganese dioxide and of LiMn$_2$O$_4$. Z Kristallogr 209:941–945. https://doi.org/10.1524/zkri.1994.209.12.941

Galwey AK (2006) What theoretical and/or chemical significance is to be attached to the magnitude of an activation energy determined for a solid-state decomposition? J Therm Anal Calorim 86:267–286. https://doi.org/10.1007/s10973-005-7157-y

Galwey AK, Brown ME (2002) Application of the Arrhenius equation to solid state kinetics: can this be justified? Thermochim Acta 386:91–98. https://doi.org/10.1016/S0040-6031(01)00769-9

Gualtieri AF (2000) Accuracy of XRPD QPA using the combined Rietveld-RIR method. J Appl Cryst 33:267–278. https://doi.org/10.1107/S002188989901643X

Hancock JD, Sharp JH (1972) Method of comparing solid-state kinetic data and its application to the decomposition of kaolinite, brucite and BaCO$_3$. J Am Ceram Soc 55:74–77. https://doi.org/10.1111/j.1151-2916.1972.tb11213.x

Hu C, Liu P, Liu Y (2011) High temperature X-ray diffraction studies of the sample heating units. Proced Eng 24:404–411. https://doi.org/10.1016/j.proeng.2011.11.2666

Johnson WA, Mehl RF (1939) Reaction kinetics in processes of nucleation and growth. Trans Am Inst Min Metall Eng 135:416–442

Kennedy BJ (2019) Thermal expansion of pyrolusite, β-MnO$_2$; a synchrotron X-ray diffraction study. J Phys Chem Solids 125:131–134. https://doi.org/10.1016/j.jpcs.2018.09.029

Khawam A, Flanagan DR (2006) Solid-state kinetic models: basics and mathematical fundamentals. J Phys Chem 110:17315–17328. https://doi.org/10.1021/jp062746a

Klingsberg C, Roy R (1959) Stability and interconvertibility of phases in the system Mn–O-OH. Am Miner 44:819–838

Kohler T, Armbruster T, Libowitzky E (1997) Hydrogen bonding and Jahn-Teller distortions in groutite, α-Mn00H, and manganite, γ-MnOOH, and their relations to the manganese dioxides ramsdellite and pyrolusite. J Solid State Chem 133:486–500. https://doi.org/10.1006/jssc.1997.7516

Kondrashev YD, Zaslavskii AI (1951) The structure of the modifications of manganese oxide. Izv Akad Nauk SSSR 15:179–186

L'vov BV (2017) Ups and downs in the theory of thermal decomposition of solids for 130 years. J Therm Anal Calorim 128:593–600. https://doi.org/10.1007/s10973-017-6200-0

MacLean LAH, Tye FL (1996) The structure of fully H-inserted γ-manganese dioxide compounds. J Solid State Chem 123:150–160. https://doi.org/10.1006/jssc.1996.0163

MacLean LAH, Poinsignon C, Amarilla JM, Le Cras F, Strobel P (1995) Electrochemical behaviour of natural and synthetic ramsdellite. J Mater Chem 5:1183–1189. https://doi.org/10.1039/JM9950501183

Miura H, Kudou H, Choi JH, Hariya Y (1990) The crystal structure of ramsdellite from Pirika Mine. J Fac Sci Hokkaido Univ Geol Min 22(4):611–617

Post JE, Heaney PJ (2004) Neutron and synchrotron X-ray diffraction study of the structures and dehydration behaviors of ramsdellite and "groutellite." Am Miner 89:969–975. https://doi.org/10.2138/Am-2004-0706

Ramsdell LS (1932) An X-ray study of psilomelane and wad. Am Miner 17:143–149

Russo M (2007) Programma per la gestione della collezione DB_AMI 2007 (DB_AMI 2007: handling software for collections). Micro 5:13–16 (**Periodico AMI, ISSN 1724-7438, Devesi-Ciriè, Torino**)

Sheldrick GM (2008) A short history of SHELX. Acta Cryst A64:112–122. https://doi.org/10.1107/S0108767307043930

Toby BH, Von Dreele RB (2013) GSAS-II: the genesis of a modern open-source all purpose crystallography software package. J Appl Cryst 46:544–549. https://doi.org/10.1107/S0021889813003531

Turner S, Buseck PR (1983) Defects in nsutite (γ-MnO_2) and dry-cell battery efficiency. Nature 304:143–146. https://doi.org/10.1038/304143a0

Wilkinson WH, Williams C, Allgood RW, Allgood GM (1983) Ramsdellite from mistake mine. Miner Rec 14:333–335

Wojdyr M (2010) Fityk: a general-purpose peak fitting program. J Appl Cryst 43:1126–1128. https://doi.org/10.1107/S0021889810030499

Wyckoff RWG (1963) β phase of MnO_2, rutile structure. Crystal structures, 2nd edn. Interscience Publishers, New York, pp 239–444

Zachau-Christiansen B, West K, Jacobsen T, Skaarup S (1994) Insertion of lithium into the manganese dioxides: pyrolusite and ramsdellite. Solid State Ion 70(71):401–406. https://doi.org/10.1016/0167-2738(94)90344-1

Zaki MI, Hasan MA, Pasupulety L, Kumari K (1997) Thermochemistry of manganese oxides in reactive gas atmospheres: probing redox compositions in the decomposition course MnO_2 to MnO. Thermochim Acta 303:171–181. https://doi.org/10.1016/S0040-6031(97)00258-X